Generalized q-Sampling Imaging

Fang-Cheng Yeh, Van Jay Wedeen, and Wen-Yih Isaac Tseng*

***Abstract*—Based on the Fourier transform relation between diffusion magnetic resonance (MR) signals and the underlying diffusion displacement, a new relation is derived to estimate the spin distribution function (SDF) directly from diffusion MR signals. This relation leads to an imaging method called generalized *q*-sampling imaging (GQI), which can obtain the SDF from the shell sampling scheme used in *q*-ball imaging (QBI) or the grid sampling scheme used in diffusion spectrum imaging (DSI). The accuracy of GQI was evaluated by a simulation study and an *in vivo* experiment in comparison with QBI and DSI. The simulation results showed that the accuracy of GQI was comparable to that of QBI and DSI. The simulation study of GQI also showed that an anisotropy index, named quantitative anisotropy, was correlated with the volume fraction of the resolved fiber component. The *in vivo* images of GQI demonstrated that SDF patterns were similar to the ODFs reconstructed by QBI or DSI. The tractography generated from GQI was also similar to those generated from QBI and DSI. In conclusion, the proposed GQI method can be applied to grid or shell sampling schemes and can provide directional and quantitative information about the crossing fibers.**

***Index Terms*—Diffusion magnetic resonance imaging (MRI), diffusion *q*-space imaging, generalized *q*-sampling imaging, quantitative anisotropy.**

I. Introduction

DIFFUSION magnetic resonance imaging (MRI) has been shown to characterize diffusion displacement of water molecules and reveal the underlying microstructure [1], [2]. The diffusion pattern can be modeled by the diffusion tensor [3], [4], which is able to demonstrate the gross fiber orientation and provide quantitative indices such as fractional anisotropy (FA) and diffusivity [5], [6]. As diffusion tensor imaging (DTI) has been widely applied in clinical research, studies have also shown that the tensor model cannot resolve the regions with complex fiber orientations, such as crossing or branching patterns [7], [8]. To better characterize the complicated fiber patterns and discern fiber orientations, several methods have been proposed, and these methods can be categorized into model-based methods and model-free methods.

Manuscript received January 26, 2010; revised March 02, 2010; accepted March 02, 2010. Date of publication March 18, 2010; date of current version September 01, 2010. This work was supported by the National Science Council, Taiwan (NSC95-2752-M-002-018-PAE). *Asterisk indicates corresponding author.*

F.-C. Yeh is with the Department of Biomedical Engineering, Carnegie Mellon University, Pittsburgh, Pennsylvania, PA 15213 USA (e-mail: frankyeh@cmu.edu).

V. J. Wedeen is with the Martinos Center for Biomedical Imaging, Department of Radiology, Massachusetts General Hospital, Harvard Medical School, Charlestown, MA 02129 USA (e-mail: van@nmr.mgh.harvard.edu).

*W.-Y. I. Tseng is with the Department of Medical Imaging, National Taiwan University Hospital, Taipei 100, Taiwan (e-mail: wytseng@ntu.edu.tw).

Color versions of one or more of the figures in this paper are available online at http://ieeexplore.ieee.org.

Digital Object Identifier 10.1109/TMI.2010.2045126

Similar to the DTI approach, model-based methods rely on a more complex model to characterize the diffusion MR signals acquired by high angular resolution diffusion imaging (HARDI), a scheme that samples data on a shell in the diffusion-encoding space, dubbed q-space [9]. These model-based methods include the multiple Gaussian model [9]–[11], generalized diffusion tensor [12], [13], spherical harmonic decomposition [14], continuous axially symmetric tensors [15], composite hindered and restricted model [16], [17], diffusion kurtosis model [18]–[20], and spherical harmonic deconvolution [21]–[24]. These methods can delineate crossing patterns and estimate the directions of crossing fibers. The resolved fiber directions can be used in fiber tracking and may facilitate the mapping of brain connectivity [25].

Model-free methods, also called q-space imaging methods, are based on the Fourier transform relation between the diffusion MR signals and the underlying diffusion displacement [26]. These methods tackle the problem by acquiring the orientation distribution function (ODF) of the diffusion displacement. From the ODF, the underlying crossing patterns of the fibers can be inferred and the microstructure property evaluated in terms of generalized fractional anisotropy (GFA) [27], [28] or diffusion anisotropy [29]. Several q-space reconstruction methods have been proposed to reconstruct ODF from diffusion MR signals. Tuch introduced q-ball imaging (QBI) [27], which uses Funk–Radon transform to reconstruct ODF from a HARDI shell dataset. The Funk–Radon transform relation constitutes the basis of the QBI reconstruction method and led to further studies that reconstructed QBI through spherical harmonic decomposition to achieve better accuracy and efficiency [30], [31]. Another q-space imaging method, diffusion spectrum imaging (DSI) [32], [33], was also proposed as a way to reconstruct ODF from MR signals. The diffusion data of DSI were acquired by grid sampling scheme, and the Fourier transform was applied to the q-space data to estimate the underlying diffusion displacement pattern for further calculation of the ODF.

Although all q-space imaging methods are able to measure diffusion ODF, some limitations still exist. The Funk–Radon transform relation proposed in the QBI method only partially exploits the relation between the MR signals and diffusion displacements. This limitation is obvious because the acquired diffusion MR signal is in fact contributed by the diffusion displacements in all directions, not just the displacements perpendicular to the diffusion gradient vector. As a result, the q-ball ODF may not be an accurate ODF that considers all diffusion displacements, as pointed out by Barnett *et al.* [34]. On the other hand, DSI is able to characterize the diffusion probability density function (PDF) by applying the Fourier transform to the MR signals in the q-space; however, it still relies on numerical estimation to get the ODF. The estimation often encounters the truncation artifacts in the Fourier transform, and a Hanning filter

is often needed to smooth the PDF [35], [36]. These numerical errors can be minimized if the ODF can be estimated directly from the measured MR signals.

In view of these limitations, we investigated the Fourier transform relation between the diffusion MR signals and the diffusion displacement of the spins, thereby deriving a new relation between spin distribution function (SDF) and the MR signals. Unlike the diffusion ODF, which is a probability distribution of the diffusion displacement, the SDF represents a quantitative distribution of the spins undergoing diffusion and can be compared across different voxels. This finding led to a generalized q-sampling imaging method (GQI), which could be applied to a wide range of q-space datasets, such as those acquired by the shell or grid sampling schemes. In this study, we conducted a simulation study and an *in vivo* study to examine the accuracy of GQI in comparison with QBI and DSI. A new quantitative index was also investigated in the simulation study, revealing its relation with fiber volume fraction.

II. Materials and Methods

A. Theory

Combined k-space and q-space imaging is based on the Fourier transform relation between the diffusion MR signals $S(\mathbf{k},\mathbf{q})$, spin density $\rho(\mathbf{r})$, and the average propagator $p\Delta(\mathbf{r},\mathbf{R})$ in the diffusion time Δ [26]

$$S(\mathbf{k},\mathbf{q}) = \int \rho(\mathbf{r}) \exp(i2\pi\mathbf{k}\cdot\mathbf{r}) \int p_\Delta(\mathbf{r},\mathbf{R}) \exp(i2\pi\mathbf{q}\cdot\mathbf{R}) d\mathbf{R} d\mathbf{r} \quad (1)$$

where $\mathbf{r}$ is the voxel coordinate, $\mathbf{R}$ is the diffusion displacement, $\mathbf{q} = \gamma\mathbf{G}\delta/2\pi$, with γ being the gyromagnetic ratio of protons, and $\mathbf{G}$ and δ being the strength and duration of the diffusion-encoding gradient, respectively. The k-space reconstruction gives us diffusion weighted image data $W(\mathbf{r},\mathbf{q})$, which reveals the underlying average propagator $p_\Delta(\mathbf{r},\mathbf{R})$ of each observed voxel

$$W(\mathbf{r},\mathbf{q}) = \int \rho(\mathbf{r}) p_\Delta(\mathbf{r},\mathbf{R}) \exp(i2\pi\mathbf{q}\cdot\mathbf{R}) d\mathbf{R}. \quad (2)$$

To represent the average propagator in the scale of spin quantity, we introduce a spin density function $Q(\mathbf{r},\mathbf{R})$, which is estimated by scaling the average propagator $p_\Delta(\mathbf{r},\mathbf{R})$ with the density function $\rho(\mathbf{r})$; i.e., $Q(\mathbf{r},\mathbf{R}) = \rho(\mathbf{r}) p_\Delta(\mathbf{r},\mathbf{R})$. Because $Q(\mathbf{r},\mathbf{R})$ is real, $W(\mathbf{r},\mathbf{q})$ is symmetric in the q-space, i.e., $W(\mathbf{r},\mathbf{q}) = W(\mathbf{r},-\mathbf{q})$. The spin density function $Q(\mathbf{r},\mathbf{R})$ can be calculated by applying the cosine transform on $W(\mathbf{r},\mathbf{q})$

$$Q(\mathbf{r},\mathbf{R}) = \int W(\mathbf{r},\mathbf{q}) \cos(2\pi\mathbf{q}\cdot\mathbf{R}) d\mathbf{q}. \quad (3)$$

We further estimate the quantity of spins that undergo the diffusion in a particular direction $\hat{\mathbf{u}}$, resulting in the SDF $\psi_Q(\mathbf{r},\hat{\mathbf{u}})$

$$\psi_Q(\mathbf{r},\hat{\mathbf{u}}) = \int_0^{L_\Delta} Q(\mathbf{r}, L\hat{\mathbf{u}}) dL \quad (4)$$

where L_Δ is the diffusion sampling length. Equation (4) shows that SDF is an orientation distribution function of the spin quantity because it is obtained from the spin density function $Q(\mathbf{r},\mathbf{R})$. SDF is also equal to diffusion ODF multiplied by the spin density. By including the spin density, the values of SDF have a unified reference, thus offering the possibility of comparing the distribution values across different voxels. In our *in vivo* experiment, the diffusion weighted images had a heavy T_2-weighted effect because the echo time was around 100 ms. To eliminate the T_2 effect and obtain more accurate estimation of SDF, each diffusion weighted image could be divided by the b0 image and then multiplied by a proton density map.

Combining (3), (4), and integrating the distance parameter L from 0 to L_Δ, we obtain the relation between the acquired diffusion weighted images $W(\mathbf{r},\mathbf{q})$ and SDF

$$\begin{aligned}\psi_Q(\mathbf{r},\hat{\mathbf{u}}) &= \int_0^{L_\Delta} \int W(\mathbf{r},\mathbf{q}) \cos(2\pi L\mathbf{q}\cdot\hat{\mathbf{u}}) d\mathbf{q} dL \\ &= L_\Delta \int W(\mathbf{r},\mathbf{q}) \mathrm{sinc}(2\pi L_\Delta \mathbf{q}\cdot\hat{\mathbf{u}}) d\mathbf{q} \end{aligned} \quad (5)$$

where $\mathrm{sinc}(x) = \sin(x)/x$ for all x except 0, and $\mathrm{sinc}(0) = 1$. Equation (5) shows that the overall SDF is composed of a series of basis SDFs in the form of sinc functions weighted by $W(\mathbf{r},\mathbf{q})$. The shape of the basis SDF is determined by the value of $|\mathbf{q}|L_\Delta$. A higher value of $|\mathbf{q}|L_\Delta$ presents a sharper contour, and vice versa. Equation (5) allows us to calculate the summation of all the basis SDFs offered by a sampling scheme, yielding the measured SDF $\psi_m(\mathbf{r},\hat{\mathbf{u}})$

$$\psi_m(\mathbf{r},\hat{\mathbf{u}}) = A_q L_\Delta \sum_{\mathbf{q}} W(\mathbf{r},\mathbf{q}) \mathrm{sinc}(2\pi L_\Delta \mathbf{q}\cdot\hat{\mathbf{u}}) \quad (6)$$

where A_q is a constant area term for the quadrature. Equation (6) is the theoretical basis of the GQI reconstruction method, which is applicable to any diffusion sampling scheme. Furthermore, the SDF can be scaled by a constant value Z_0 such that the SDF of pure water diffusion is 1. To estimate the Z_0, in practice, the SDF of cerebrospinal fluid (CSF) could be used as a reference because CSF resembles free diffusion of pure water.

Note that this SDF scaling is different from the ODF normalization used in QBI and DSI. The ODF normalization is performed independently for each voxel to fulfill the requirement of a probability density function. The SDF scaling, instead, is applied to all voxels simultaneously, and thus the scaled SDFs can still be compared across different voxels. Nonetheless, if diffusion ODF is preferred, normalizing the SDF will turn it into the diffusion ODF.

B. The Relation With Other q-Space Methods

Comparing the reconstruction equations of GQI and QBI, we found that if the diffusion sampling length L_Δ in (5) is set to infinity, the sinc function in the equation approximates a delta function, resulting in the same Funk–Radon transform used by QBI. Such a feature leads us to suggest that QBI could be viewed as a special case of GQI that has an infinite diffusion sampling length, and GQI is a general approach that allows a finite diffusion sampling length.

On the other hand, GQI and DSI also share the same theoretical basis: the Fourier transform relation between the diffusion MR signals and the underlying diffusion displacement. This may suggest that the GQI and DSI reconstruction could result in similar diffusion patterns. However, they still differ in their numerical approaches. In DSI, Fourier transform is applied

to the q-space data, and then the diffusion ODF is calculated by the numerical integration on the transformed grid data. GQI, instead, is based the result of the mathematical reduction that combines the Fourier transform and ODF calculation, thereby deriving a direct relation between the diffusion signal and SDF. Such an approach avoids the procedures of Fourier transform and the subsequent interpolation on the grid data points.

Another difference between DSI and GQI is their ODF regularization approaches. DSI reconstruction often relies on a Hanning filter to reduce the truncation artifact in Fourier transform, an artifact that gives rise to a spiky appearance in the ODF. GQI, instead, offers an explicit control parameter L_Δ to minimize the artifact. Though it is not clear which approach leads to better angular resolution, the explicit parameter L_Δ provided by GQI ensures that the reconstruction can be reproduced exactly for further comparison with other methods.

Yet another major difference between DSI and GQI is that the definition of ODF in DSI includes a distance weighting L^2

$$\psi(\hat{\mathbf{u}}) = \int_0^\infty p_\Delta(L\hat{\mathbf{u}})L^2 dL. \tag{7}$$

This weighting term is a Jacobian determinant that results from transforming the average propagator p_Δ to the diffusion ODF. We can further apply mathematical reduction to simplify the numerical integration in (7) and obtain a different basis function for GQI

$$\psi_m(\mathbf{r},\hat{\mathbf{u}}) = A_q L_\Delta^3 \sum_{\mathbf{q}} W(\mathbf{r},\mathbf{q}) f(2\pi L_\Delta \mathbf{q}\cdot\hat{\mathbf{u}})$$
$$f(x) = \begin{cases} \frac{2\cos(x)}{x^2} + \frac{(x^2-2)\sin(x)}{x^3}, & x \neq 0 \\ \frac{1}{3}, & x = 0 \end{cases} \tag{8}$$

where $f(x)$ is the basis SDF resulted from the L^2 weighting. Nonetheless, there is no guarantee of which weighting approach is a better estimation for fiber orientations. The accuracy for different L weighting strategies requires further investigation. In this study, the GQI reconstruction only used the sinc function as the basis function for reconstruction.

C. Diffusion Sampling Length

The value of the diffusion sampling length L_Δ in (4) offers a way to adjust the range of diffusion displacement to be integrated. A lower L_Δ covers spins with less diffusion displacement, resulting in coarser SDFs. A higher L_Δ, on the other hand, covers a larger range and results in sharper SDFs. With such features, L_Δ can serve as a regularization parameter to adjust the coarseness of the SDF.

The choice of L_Δ can be made by estimating the diffusion length. If the underlying diffusion follows Gaussian distribution, the diffusion length is $(6\mathrm{D}\tau)^{1/2}$, where D is the diffusion coefficient and τ the effective diffusion time $\tau = (\Delta - \delta/3)$. The diffusion length can be used as the unit of L_Δ, i.e., $L_\Delta = \sigma(6\mathrm{D}\tau)^{1/2}$, where σ is an adjustable factor. If we choose $\sigma = 1.25$, then 80% of the diffusion distribution will be encompassed in the SDF. Under the restricted diffusion condition, the percentage of coverage will even be higher. From experience, we found that setting σ between 1 and 1.3 yields good reconstruction results. A σ higher than 1.3 may increase the sensitivity to noise and makes the reconstruction unfavorable.

The introduction of the σ has another benefit. We can replace the L_Δ in (6) by $\sigma(6\mathrm{D}\tau)^{1/2}$, resulting in the following reconstruction equation:

$$\psi_m(\mathbf{r},\hat{\mathbf{u}}) = A_q L_\Delta \sum_{\mathbf{q}} W(\mathbf{r},\mathbf{q}) \mathrm{sinc}\left(\sigma\sqrt{6D\cdot b(\mathbf{q})}\cdot\frac{\mathbf{q}}{|\mathbf{q}|}\cdot\hat{\mathbf{u}}\right) \tag{9}$$

where $b(\mathbf{q})$ is the b-value of the corresponding diffusion encoding $\mathbf{q}$, for $b(\mathbf{q}) = (2\pi|\mathbf{q}|)^2\tau$, and $\mathbf{q}/|\mathbf{q}|$ is the diffusion gradient direction in unit vector. This reconstruction equation uses b-values and σ as the input instead of the q values. Since the b-value is commonly used in most diffusion pulse sequences, it is more convenient to use (9) to perform GQI reconstruction.

D. Applicable Sampling Schemes

Although GQI can be applied to any sampling schemes to reconstruct SDF, the reconstruction result may not be correct if a sampling scheme is not balanced. One way to check this condition is to test whether the sampling scheme fulfills the balanced requirement: the MR signals obtained from an isotropic diffusion should be reconstructed to an isotropic SDF. Under this paradigm, we propose a quick numerical test to check whether a sampling scheme is acceptable for GQI reconstruction. Assuming that the numerical MR signals are generated from an isotropic diffusion tensor $\mathrm{D_I}$, we expect the MR signal to be reconstructed to an isotropic SDF, which can be calculated by the following formula, where τ is the effective diffusion time

$$\psi_0(\hat{\mathbf{u}}) = A_q L_\Delta \sum_{\mathbf{q}} \mathrm{sinc}(2\pi L_\Delta \mathbf{q}\cdot\hat{\mathbf{u}}) \exp(-4\pi^2 \mathbf{q}^T \mathrm{D_I}\mathbf{q}\tau). \tag{10}$$

To fulfill the balanced requirement, the reconstructed SDF $\psi_0(\hat{\mathbf{u}})$ should be nearly isotropic, which can be examined by calculating the variance of the SDF. The balanced requirement provides a framework to design an acceptable sampling scheme, thereby facilitating the development of a GQI sampling scheme that is optimized for clinical use. Also, this requirement can be used as a necessary condition for obtaining correct reconstruction; however, further study is still needed to determine whether this requirement is sufficient.

E. Quantitative Anisotropy of the Spin Distribution

In this paper, we defined an index called quantitative anisotropy (QA) to quantify the spin population in a specific direction. Unlike FA or GFA, which is a metric for each voxel, QA is a metric for each resolved fiber population. This allows QA to be compared to fiber specific information such as the volume fraction of each individual fiber. The QA in a resolved fiber orientation is defined by the SDF value at the resolved fiber orientation $\hat{\mathbf{a}}$ minus the background isotropic diffusion component $\mathrm{I}(\psi_Q)$

$$QA(\hat{\mathbf{a}}) = Z_0\left(\psi_Q(\hat{\mathbf{a}}) - \mathrm{I}(\psi_Q)\right) \tag{11}$$

where Z_0 is the SDF scaling constant. To estimate the isotropic component, in this study, we used the minimum value of ψ_Q as an approximation.

F. Simulation Study

We performed a simulation study to validate the accuracy of GQI by comparing it with QBI and DSI. The simulation model was based on a mixed Gaussian model consisting of a component of isotropic diffusion and two fiber populations [9], [14]

$$\mathrm{S}(b,\mathbf{v}) = S(0)(f_1 \exp[-b\mathbf{v}^{\mathbf{T}}\mathrm{D}_1\mathbf{v}] + f_2 \exp[-b\mathbf{v}^{\mathbf{T}}\mathrm{D}_2\mathbf{v}] + f_0 \exp[-b\mathbf{v}^{\mathbf{T}}\mathrm{D}_0\mathbf{v}]) \quad (12)$$

where b and $\mathbf{v}$ are the b-value and the unit vector of the applied diffusion gradient, respectively, f_1 and f_2 the volume fractions of the two fiber populations, and f_0 is the volume fraction of the isotropic diffusion. D_0, D_1, and D_2 are the diffusion tensor matrices for these three diffusion components. We simulated this model with a variety of parameter combinations so that we would not have bias on any parameter. Also, to decouple the relation between f_1 and f_2, we also added various volume fractions of background isotropic diffusion in the simulation model, the f_0. The simulation model was then used to generate diffusion weighted images with noise added. The images followed the same reconstruction flow as the practical condition. In the simulation study, the f_0 was 0.1, 0.2, 0.3, 0.4, and 0.5. The volume fractions of the major fibers were assigned from $0.5 \times (1 - f_0)$ to $1.0 \times (1 - f_0)$, which was further divided into 64 divisions. The remaining volume was occupied by the minor fiber population. The crossing angles between major and minor fibers ranged from 30° to 90°, divided into 64 divisions. The mean diffusivity was 1.0×10^{-3} mm^2/s, and the FA values for both of the simulated fibers were 0.3, 0.4, 0.5, and 0.6. A total of 81 920 parameter combinations were simulated with Rician noise [37] added under $\mathrm{b0\text{-}SNR} = 30$. Each parameter combination further underwent five simulation trials, resulting in 409 600 simulation scenarios. For QBI, each simulation scenario generated 252 MR signals according to a 252-direction b-table with b-value $= 3000$ s/mm^2. The sampling directions of the b-table were obtained from a five-fold tessellated icosahedron. For DSI, a 203-point grid sampling scheme with a maximum b-value of 4000 s/mm^2 was used to generate the MR signals. The grid sampling points were obtained by iterating the integrals q_x, q_y, and q_z satisfying $q_x^2 + q_y^2 + q_z^2 \leqq 13$, which is according to the optimum sampling scheme recommended by Kuo *et al.* [36].

The simulated QBI signals were reconstructed by the spherical harmonic approach [31] with a regularization term based on the Laplace–Beltrami operator. As recommended by Descoteaux *et al.* [31], the spherical harmonic order was set to 8 and the regularization parameter was set to 0.006. The obtained ODF had 362 directions generated from a six-fold tessellated icosahedron, offering an angular resolution of around 9°. The simulated DSI signals were placed in a $16 \times 16 \times 16$ matrix (q value $= -8$ to 7) with zero padding. To eliminate truncation artifacts, smoothing was performed by applying a Hanning filter of cosine $(2\pi\, q/16)$, where q was the q-space distance from the origin, as proposed in an optimization study [36]. The diffusion PDF was obtained by discrete Fourier Transform and transformed into a 362-direction ODF by integration in each sampling direction. Both QBI and DSI datasets were also reconstructed by GQI method with diffusion sampling lengths L_Δ of 35, 45, 55, and 65 μm, under the assumption that the diffusion time was 80 ms (diffusion length$= 32$ μm). The q-values were estimated from the b-values by assuming that the diffusion gradient duration δ was 35 ms and that the MR signals were obtained using a standard pulsed-gradient spin-echo pulse sequence, where $b = (\gamma \mathrm{G}\delta)^2(\Delta - \delta/3)$ and $q = \gamma \mathrm{G}\delta/2\pi$. Using the reconstruction methods mentioned above, the fiber orientations were determined by the local maxima of the reconstructed ODFs or SDFs.

The performance of a reconstruction method was evaluated by its ability in resolving major and minor fibers. The major fiber was defined by the largest local maximum (the global maximum) on a SDF or ODF. The minor fiber was defined by the second largest local maximum. In this study, we limited the fiber population in the two-fiber condition to simplify comparison.

To evaluate the ability to resolve major fibers, we calculated the average of the angular deviation, which was the inner angle between the resolved fiber orientation and the actual orientation. A lower value in the average angular deviation suggested better performance.

Evaluating the ability to resolve minor fibers is more complicated. A reconstruction may fail to resolve the minor fiber, and the angular deviation cannot be calculated. Also, inadequate smoothing could result in false minor fibers that present a spurious increase in performance. To avoid giving credit to false fibers and to handle the situation of missing fibers, we defined a condition called "successful resolving," which only gives credit to the cases in which minor fibers were accurately resolved. When the resolved orientation was in the same discrete orientation as the actual one, the condition was counted as "success;" on the contrary, when the minor fiber could not be identified or the resolved orientation was not the same as the actual one, the condition was counted as "failure." The performance of a method was then evaluated by the percentage of successful trials. Higher percentages indicated better performance.

One should note that the fiber orientations are discretized to 362 sampling orientations, so the same orientation occurring in the "success" condition implies that the angular deviation of the resolved minor fiber is less than a half of the ODF resolution, approximately 4°–5°. Therefore, it is expected that the percentage of successes may not be high.

G. In Vivo Experiments

A 27-year-old volunteer without any known neurological disease was scanned on a 3T scanner (TIM Trio, Siemens, Erlangen, Germany). The subject signed an informed consent form approved by the institutional review board. The scan was done with a single-shot twice-refocused echo planar imaging (EPI) diffusion pulse sequence and a 12-channel head coil. The field of view was 240×240 mm, matrix size 96×96, slice thickness 2.5 mm (no gap), number of slices 40, and voxel size $2.5 \times 2.5 \times 2.5$ mm. Under the prescribed spatial parameters, a 252-direction shell sampling scheme and a 203-point grid sampling scheme were scanned subsequently. For the 252-direction shell scheme, the b-value $= 4000$ s/mm^2, TR/TE $= 7200/133$ ms, average number $= 1$, resulting in a scanning time of 30 min. For the 203-point grid scheme, the maximum b-value $= 5000$ s/mm^2, TR/TE $= 7200/144$ ms,

resulting in a scanning time of 25 min. The dataset acquired by the 252-direction shell sampling scheme was reconstructed separately by spherical harmonic based QBI and GQI, and the dataset obtained from the 203-point grid sampling scheme was reconstructed separately by DSI and GQI. The reconstruction methods were applied to each dataset using the same parameter settings as the simulation study, and 40 μm ($\sigma = 1.25$) was adopted as the diffusion sampling length for GQI reconstruction.

The *in vivo* images were also used to demonstrate the application of the balanced requirement in obtaining feasible diffusion sample schemes. First, we generated several possible schemes by subsampling the current 252-direction shell and 203-point grid dataset into fewer sampling points. The possible schemes were further checked by the balanced requirement, and the acceptable schemes were selected to receive further GQI reconstruction. Moreover, for schemes having less sampling direction, lower values of diffusion sampling length were used to fulfill the balanced requirement. The reconstructed results were then compared with the reconstruction of the original data to observe whether the SDFs were consistent.

For the 252-direction shell dataset, a total of 50 000 possible schemes were randomly generated to obtain three acceptable schemes, including 126-direction, 64-direction, and 32-direction sampling. The diffusion sampling lengths for each scheme were 25.6 μm ($\sigma = 0.8$), 19.2 μm ($\sigma = 0.6$), and 12.8 μm ($\sigma = 0.4$), respectively.

For the 203-point grid dataset, the dataset was first subsampled into a half sphere, which had 102 points in q-space. Possible schemes were generated by discarding different amounts of the high b-value data. Three acceptable subsampled schemes were obtained for further reconstruction, including 102-point ($b\text{-}\max = 5000\ \mathrm{s/mm^2}$), 41-point ($b\text{-}\max = 2307\ \mathrm{s/mm^2}$), and 17-point ($b\text{-}\max = 1538\ \mathrm{s/mm^2}$) sampling. The diffusion sampling lengths for each scheme were 32 μm ($\sigma = 1.0$), 25.6 μm ($\sigma = 0.8$), and 19.2 μm ($\sigma = 0.6$), respectively.

H. Tractography Study

The tractography of QBI, DSI, and GQI was obtained by a modified streamline tracking algorithm implemented on the in-house program, DSI Studio (http://dsi-studio.labsolver.org). This algorithm used Eulerian integration similar to another streamline approach [38] but was modified to make use of multiple fiber orientations at each voxel. The seeding points, which were the starting points for tracking, were uniformly distributed within a user-defined region. In this study, we placed an ovoid seeding region in the centrum semiovale. The propagation direction was calculated by applying trilinear interpolation on the fiber orientations provided from eight nearby voxels of the current point. For each nearby voxel, only the fiber orientation that had the smallest turning angle was considered for interpolation. The next point was then determined by moving in the propagation direction for 1 mm. The propagation process repeated until the tracking trajectory fulfilled either a turning angle of greater than 60° or the anisotropy value of the current position below a predefined threshold. To get a suitable anisotropy threshold for each method, the GFA or QA of the cortical area were inspected separately, and the isocontour of the threshold was adjusted to cover the same extent of the white matter area. A threshold of $\mathrm{GFA} = 0.1$ was used for QBI and DSI, and a threshold of $\mathrm{QA} = 0.07$ was used for GQI. To facilitate comparison, we further separated the generated tracts by the orientations with which they enter the seeding region. The tracts passing in the anterior–posterior and vertical directions were separated by the interactive interface on DSI Studio.

III. Results

A. Simulation Study

The results of QBI and GQI applied to the same simulated dataset are summarized in Table I and presented in Fig. 1(a) and (b). The results showed that the average major fiber deviation was $3.94° \pm 3.46°$ (mean $\pm$ standard deviation) for QBI, whereas for GQI, the deviation had a lowest value of $3.22° \pm 3.50°$ when the diffusion sampling length L_Δ was 35 μm. The angular deviation of major fibers in GQI gradually increased as L_Δ became longer. The percentage of success in resolving minor fibers was 11.08% for QBI. For GQI, that percentage had the highest value of 13.61% when $L_\Delta = 45$ μm.

The results of DSI and GQI applied to the same simulated dataset are summarized in Table II and presented in Fig. 1(c) and (d). The results showed that the average major fiber deviation was $3.15° \pm 3.29°$ for DSI. For GQI, the deviation had the lowest value, $1.05° \pm 2.55°$, when the diffusion sampling length L_Δ was 65 μm. Unlike the results shown in Table I, the angular deviation of the major fiber in GQI gradually decreased as L_Δ became longer. The percentage of success in resolving minor fibers was 8.59% for DSI. For GQI, the percentage gradually increased as L_Δ increased and achieved the highest success rate of 9.54% when $L_\Delta = 65$ μm.

To analyze the relation between QA and volume fraction, we selected the 203-point grid simulation scenarios that had $\mathrm{FA} = 0.4, 0.5,$ and 0.6, while the volume fractions of the major fiber, minor fiber, and isotropic components varied independently as described in the Method section. In the selected scenarios, we excluded the scenarios that failed to resolve fibers within 9°, resulting in a total of 31 056 simulation scenarios. We calculated the QA of each resolved fiber population and observed the correlations between QA and the assigned variables of the fiber. The correlation coefficient between QA and the fiber volume fraction was 0.8602 ($p < 0.01$); it was -0.3275 ($p < 0.01$) between QA and the volume fraction of the isotropic background; and it was 0.3812 ($p < 0.01$) between QA and FA of the fiber.

B. In Vivo Experiments

Fig. 2 presents a three-way fiber crossing region in the left hemisphere. Note that the ODFs provided by QBI [Fig. 2(a)] are similar to the SDFs offered by GQI [Fig. 2(b)], which was applied to the same dataset acquired by the shell sampling scheme. Also, the ODFs provided by DSI [Fig. 2(c)] are similar to the SDFs offered by GQI [Fig. 2(d)], applied to the same dataset acquired by the grid sampling scheme. Fig. 3 presents the reconstructed result of a two-way fiber crossing region in the right hemisphere. Likewise, the results of QBI [Fig. 3(a)]

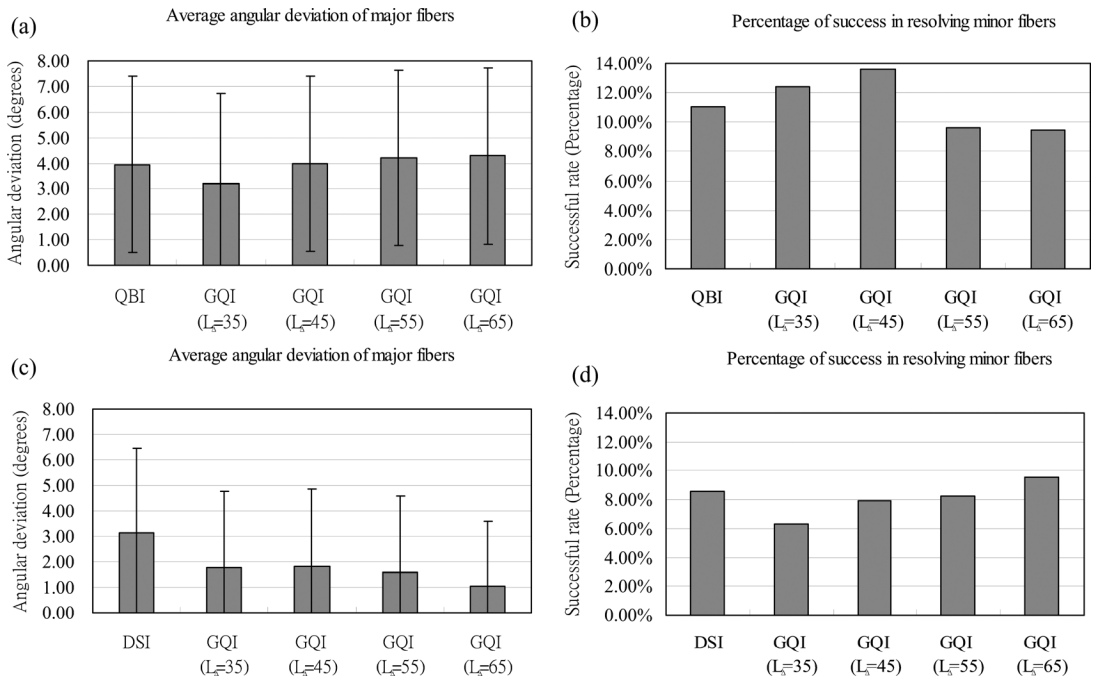

Fig. 1. Simulation results of different settings in resolving major and minor fibers. Results of QBI and GQI reconstruction methods applied to the same simulated 252-direction shell dataset: (a) the angular deviation of major fibers, and (b) the percentage of success in identifying minor fibers. Results of DSI and GQI reconstruction methods applied to the same simulated 203-point grid dataset: (c) the angular deviation of major fibers, and (d) the percentage of success in identifying minor fibers. The error bars in (a) and (c) represent the standard deviations of the major fiber deviation.

TABLE I
SUMMARY OF THE SIMULATION RESULTS

Reconstruction method	QBI	GQI (L_Δ=35μm)	GQI (L_Δ=45μm)	GQI (L_Δ=55μm)	GQI (L_Δ=65μm)
Average deviation of major fibers	$3.94^\circ \pm 3.46^\circ$	$3.22^\circ \pm 3.50^\circ$	$3.99^\circ \pm 3.42^\circ$	$4.22^\circ \pm 3.44^\circ$	$4.28^\circ \pm 3.45^\circ$
Successful resolving of minor fibers	11.08%	12.40%	13.61%	9.63%	9.47%

The reconstruction methods were applied to the same dataset simulated by the 252-direction shell sampling scheme.

TABLE II
SUMMARY OF THE SIMULATION RESULTS

Reconstruction method	DSI	GQI (L_Δ=35μm)	GQI (L_Δ=45μm)	GQI (L_Δ=55μm)	GQI (L_Δ=65μm)
Average deviation of major fibers	$3.15^\circ \pm 3.29^\circ$	$1.79^\circ \pm 3.00^\circ$	$1.84^\circ \pm 3.03^\circ$	$1.58^\circ \pm 3.02^\circ$	$1.05^\circ \pm 2.55^\circ$
Successful resolving of minor fibers	8.59%	6.33%	7.90%	8.22%	9.54%

The reconstruction methods were applied to the same dataset simulated by the 203-point grid sampling scheme.

and the results of GQI [Fig. 3(b)] are similar, as are those of DSI [Fig. 3(c)] and GQI [Fig. 3(d)].

The QA maps of the *in vivo* images are presented in Fig. 4. Fig. 4(a) and (b) show the QA maps of the major fibers, and Fig. 4(c) and (d) show the QA maps of the minor fibers. These QA maps were generated by applying the GQI reconstruction method on the *in vivo* 203-point grid dataset. The QA maps of the major fibers revealed regions with predominant fiber tracts, such as the corpus callosum, internal capsule, and cerebral peduncle, all of which showed higher QA values than other white matter regions [Fig. 4(a) and (b)]. On the other hand, the QA maps of the minor fibers revealed regions having crossing fibers, such as the pons containing pontocerebellar tracts and corticospinal tracts, and the centrum semiovale containing the corpus callosum, superior longitudinal fasciculus, and corona radiata [Fig. 4(c) and (d)].

In the balanced requirement experiment, the reconstructed SDFs of the subsampled shell dataset are presented in Fig. 5, and the reconstructed SDFs of the subsampled grid dataset are presented in Fig. 6. Both figures were focused on the same three-way crossing region in the centrum semiovale of the right hemisphere, and the SDFs of the original datasets without subsampling are also presented for comparison. As presented in Fig. 5, the 126-direction and 64-direction shell datasets had

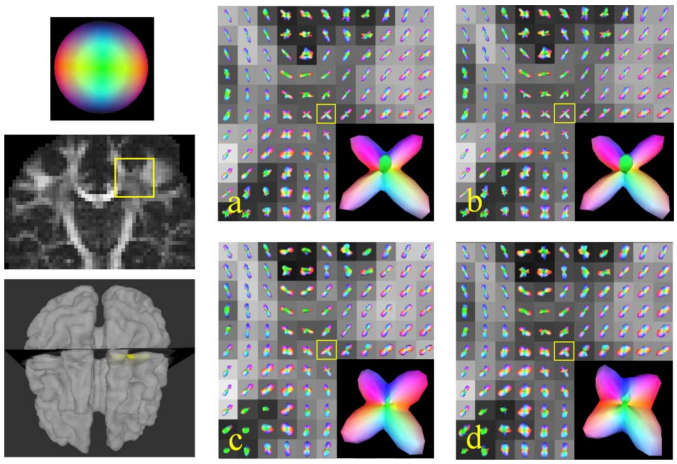

Fig. 2. Coronal view showing centrum semiovale where the callosal fibers, corticospinal tract and superior longitudinal fasciculus form a three-way crossing pattern. The slice position is indicated on the 3-D volume rendering of white matter. The ODF or SDF maps are generated by different combinations of methods and datasets. Panel (a) is the 252-direction shell dataset reconstructed by QBI, and panel (b) is the same dataset reconstructed by GQI. Panel (c) is the 203-point grid dataset reconstructed by DSI, and panel (d) is the same dataset reconstructed by GQI. The directions of the ODF or SDF are pseudo-colored: red in the left–right direction, green in the anterior-posterior direction, and blue in the axial direction. The gray-leveled background is the mapping of GFA. In each panel, a representative ODF or SDF in the same position is focused to facilitate visualization (inset).

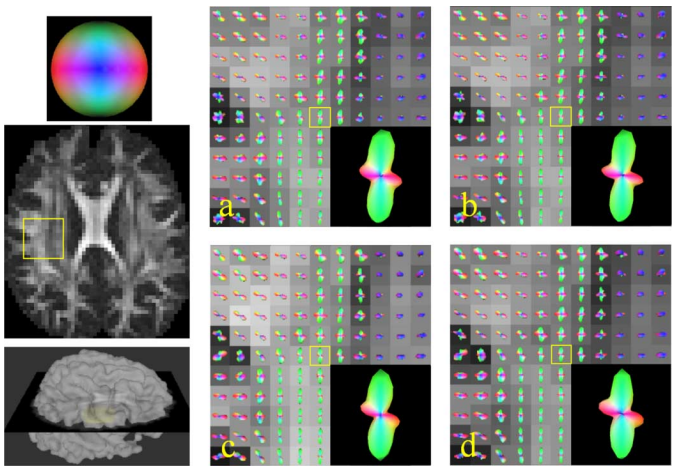

Fig. 3. Axial view of the centrum semiovale where callosal fibers and the superior longitudinal fasciculus form a two-way crossing pattern. The ODF or SDF maps are generated as follows: panel (a) is the shell dataset reconstructed by QBI, panel (b) is the same dataset reconstructed by GQI, panel (c) is the grid dataset reconstructed by DSI, and panel (d) is the same dataset reconstructed by GQI. The images are displayed in the same way as those in Fig. 2.

contours similar to the original ones, although the contours were duller. In the 32-direction dataset, although the crossing pattern was not observed in the resulted SDFs, they still maintained consistent overall orientations. Furthermore, even though the images in the 32-direction dataset were acquired by a b-value of 4000 $\mathrm{s/mm^2}$, they could only be reconstructed with a lower value of diffusion sampling length in order to fulfill the balanced requirement. As a result, the reconstructed SDFs were much duller, in the same way as the SDFs reconstructed from lower b-value images. In Fig. 6, likewise, the 102-point, 41-point, and 17-point grid datasets showed consistent overall

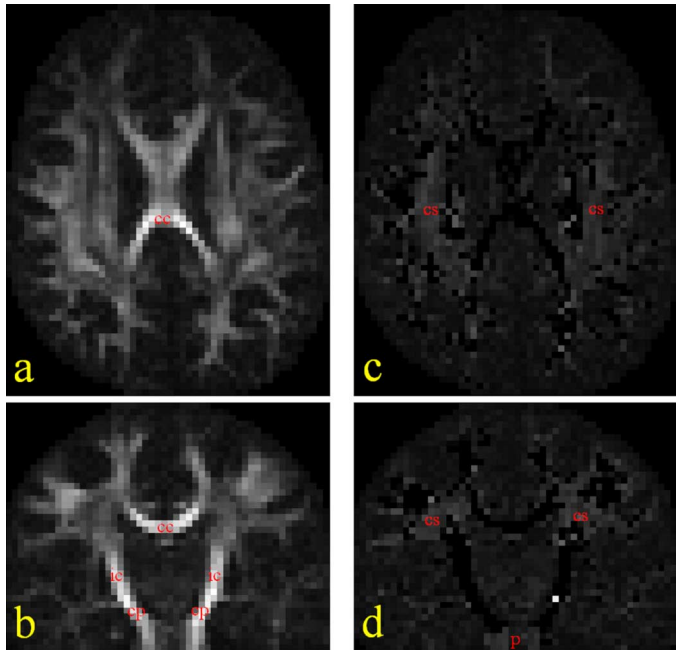

Fig. 4. Mappings of the quantitative anisotropy (QA) values of the resolved major fibers (a), (b) and the minor fibers (c), (d). The position of coronal slice and axial slice are similar to those shown in Figs. 2 and 3, respectively. Note that QA maps of the major fibers highlight the regions with predominant fiber tracts such as the corpus callosum (cc), internal capsule (ic), and cerebral peduncle (cp). QA maps of the minor fibers highlight regions with crossing fibers such as the pons (p) and centrum semiovale (cs). In the QA maps of the minor fibers, the QA value is assigned 0 if a voxel has no minor fibers.

orientations with the original ones, but appeared duller as the sampling points decreased.

C. Tractography

In this section, we present the tractography of QBI, DSI, and GQI as a qualitative comparison. The association fiber tracts that pass through the centrum semiovale are shown in Fig. 7, where directional color is used to present the local orientation of the fiber tracts. The tractography generated by QBI is presented in Fig. 7(a), and GQI applied to the same data is presented in Fig. 7(b). Similarly, the tractography generated by DSI is presented in Fig. 7(c), and GQI applied to the same data is presented in Fig. 7(d). The location of the centrum semiovale is presented by a yellow-colored region. On the left side of Fig. 7, the surface rendering of the white matter and the fiber tracts are presented together to demonstrate their relative locations. In Fig. 7(a)–(d), all the rendered tracts show a generally similar pathway; the arcuate fasciculus presents an arc-like fiber bundle connecting the Broca's and Wernicke's areas, and the termination points at the Wernicke's area present a consistent pattern. However, minor differences can still be observed among these four rendered tracts, such as fibers connecting to the angular gyrus (the green fibers that extend to the right side) or the fibers going to the Broca's area.

Fig. 8 shows the tractography of projection fiber tracts that pass through the centrum semiovale. The tractography generated by QBI is presented in Fig. 8(a), and GQI applied to the same data is presented in Fig. 8(b). The tractography generated by DSI is presented in Fig. 8(c), and GQI applied

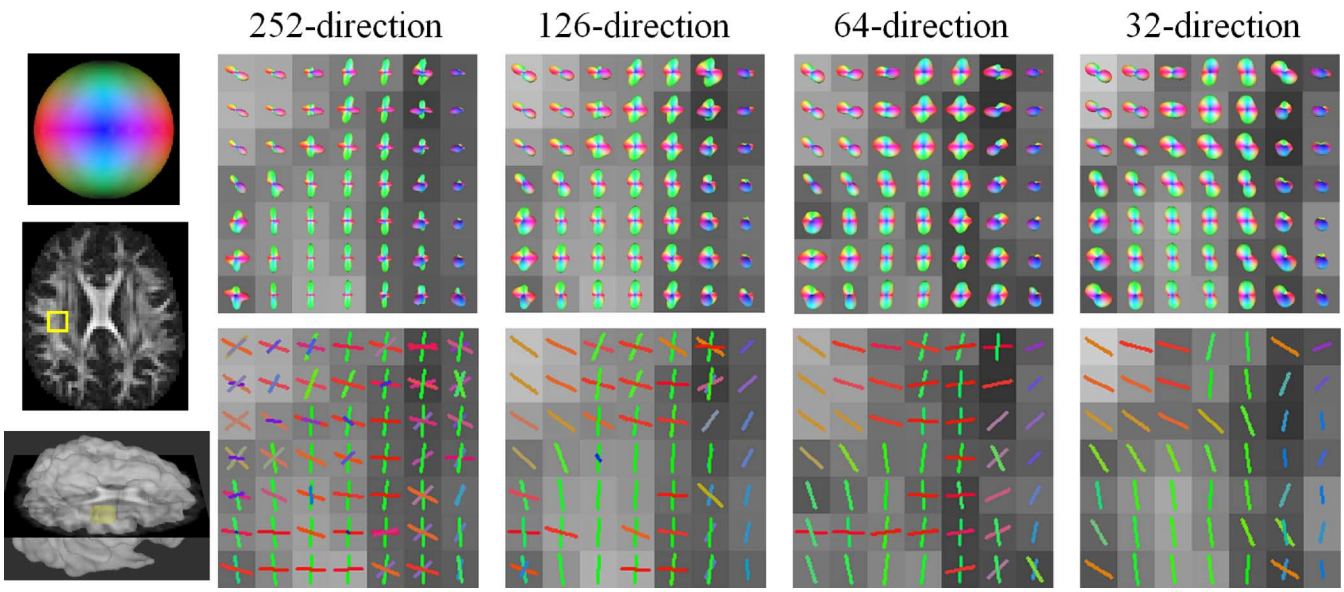

Fig. 5. Reconstruction result of GQI on subsampled shell schemes (126-direction, 64-direction, and 32-direction). The result of the original 252-direction datasets without subsampling is also presented for comparison. The SDFs of the centrum semiovale where callosal fibers and the superior longitudinal fasciculus form a two-way crossing pattern are presented in the upper row. The resolved fiber orientations of the SDFs are presented in the lower row.

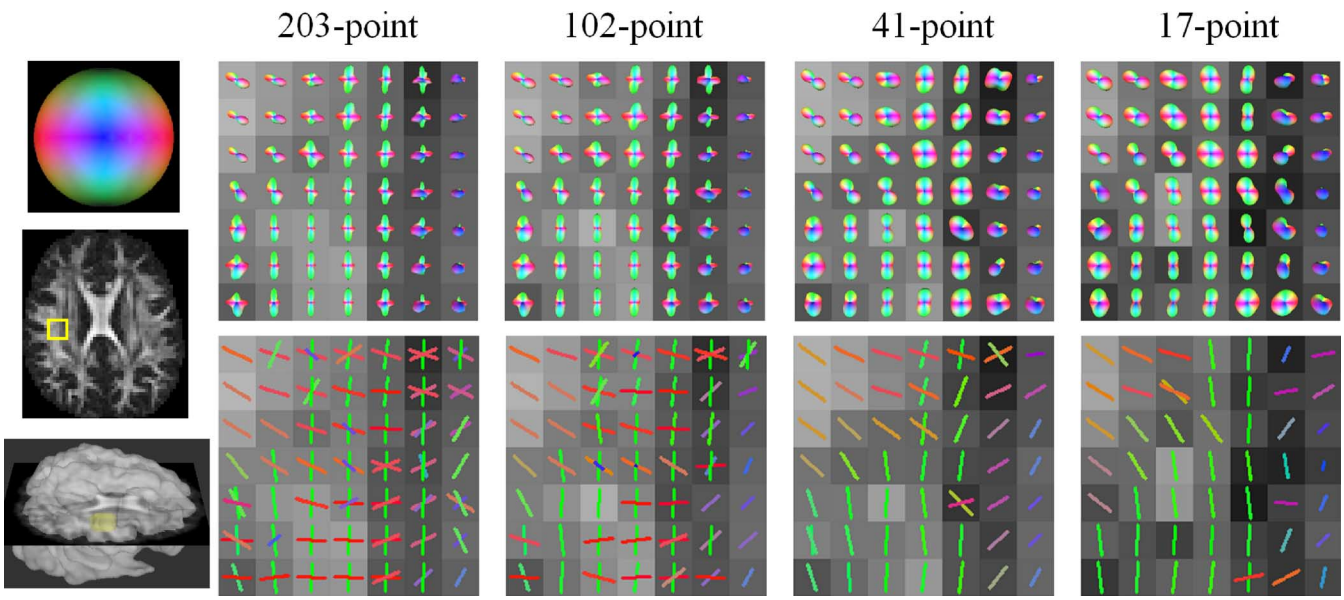

Fig. 6. Reconstruction result of GQI on subsampled grid sampling scheme (102-point, 41-point, and 17-point). The result of the original 203-point datasets without subsampling is also presented for comparison. The SDFs of the centrum semiovale in the same region as Fig. 5 are presented in the upper row. The resolved fiber orientations of the SDFs are presented in the lower row.

to the same data is presented in Fig. 8(d). The projection fiber tracts rendered by these four settings appear similar in general. Furthermore, higher similarity can be found between Fig. 8(a) and (b), as well as between Fig. 8(c) and (d). The above qualitative comparisons demonstrate that GQI applied to different sampling schemes could produce tractography similar to that reconstructed by the original reconstruction method.

IV. Discussion

In this paper, we propose a q-space imaging method called GQI, the accuracy of which was evaluated by simulation and *in vivo* studies in comparison with QBI and DSI. The simulation results showed that the accuracy of GQI in resolving major and minor fibers was comparable with that of QBI in the shell sampling scheme and that of DSI in the grid sampling scheme. The QA values, even under different FA values and isotropic volume fractions, were shown to have a close association with the volume fractions of the resolved fiber populations. The *in vivo* results showed that the SDF patterns reconstructed by GQI were similar to the ODFs reconstructed by either QBI or DSI. The QA maps of major and minor fibers also highlighted regions with predominant fiber tracts and regions with crossing fibers, respectively. The tractography study showed that GQI

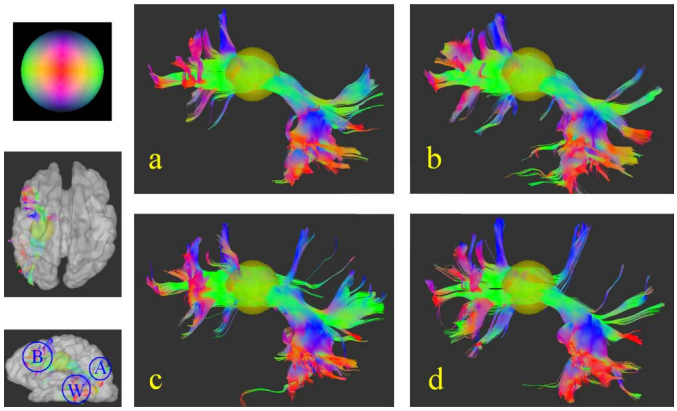

Fig. 7. The tractography of (a) QBI on 252-direction sampling scheme, (b) GQI on 252-direction sampling scheme, (c) DSI on 203-point sampling scheme, and (d) GQI on 203-point sampling scheme. The 3-D volume rendering of white matter is shown on the left with the seeding area presented by the yellow region. Only the fibers passing the seeding region in the left centrum semiovlale (yellow ovoid region) in anterior–posterior directions are presented. The locations of the Broca's area (B), Wernicke's area (W), and angular gyrus (A) are labeled on the left to illustrate their relative positions.

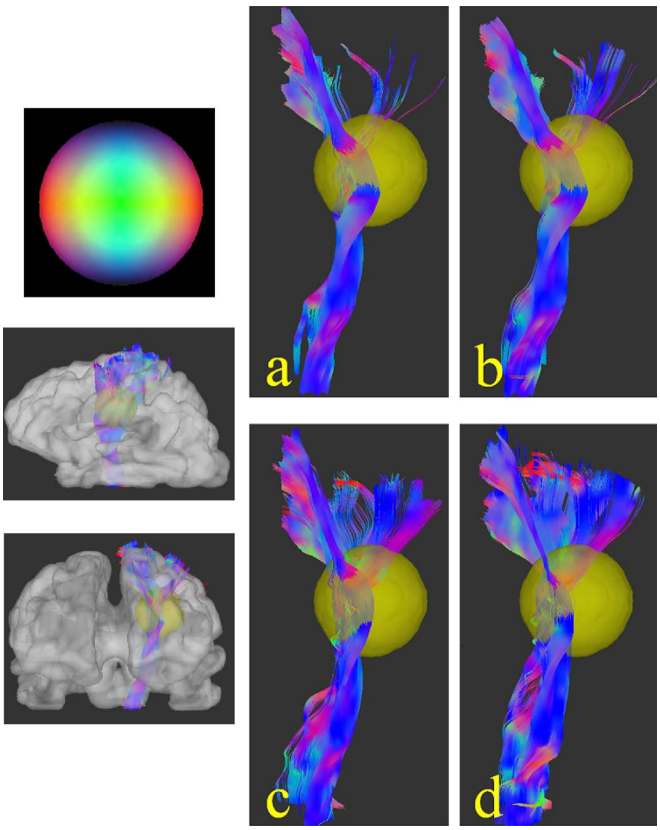

Fig. 8. The tractography of (a) QBI on 252-direction sampling scheme, (b) GQI on 252-direction sampling scheme, (c) DSI on 203-point sampling scheme, and (d) GQI on the 203-point sampling scheme. Only the fibers passing the seeding region in the left centrum semiovale (yellow ovoid region) in the vertical directions are presented.

with the modified streamline fiber tracking method was able to offer results similar to those of QBI and DSI applied on the shell and grid datasets, respectively. The minor differences in tractography resulted from the differences in reconstruction methods and sampling schemes.

In this study, we cannot say that GQI has better angular resolution than QBI and DSI. The simulation study showed that the accuracy of GQI was affected by the diffusion sampling length L_Δ. A similar scenario could also occur with QBI and DSI, considering that the reconstruction methods and parameters used in this study may not be optimal. Although we adopted one improved method for QBI reconstruction [31], [36], several alternative methods are available [27], [30], [39], [40], and no consensus has been achieved as to which method is the best. As for DSI, even though the optimum acquisition scheme has been recommended previously and was adopted in this study [36], we note that the accuracy of DSI is still influenced by the parameters of the Hanning filter used in the reconstruction process. Since the methods applied in this study might not have employed the best settings, we can only conclude that the GQI, QBI, and DSI reconstructions employed in this study have comparable accuracy in resolving crossing fibers.

Other than the consistency with other q-space methods, GQI seems to have potential advantages that may be worth noting. First, the reconstruction process of GQI does not require deconvolution procedures. The convolution feature of GQI is easy to analyze and implement. Second, the proposed method offers an opportunity to compare the SDF values amongst voxels. In QBI and DSI reconstruction, each ODF is locally normalized, and the same ODF value in different voxels does not necessarily represent the same physical quantity, making the comparison of ODFs among voxels impossible. The SDF values, instead, are calculated by scaling the average propagator with the density function, thus unifying the scale of SDF across different voxels. This approach gives the SDF a consistent physical meaning over all the voxels and therefore allows inter-voxel comparison. Finally, GQI is readily applicable to a variety of sampling schemes. In the simulation and *in vivo* studies, we have shown that GQI is generally applicable to datasets acquired by either shell or grid sampling schemes. Although not demonstrated in this study, GQI can also be applied to DTI datasets or even the combination of datasets acquired by any of the sampling schemes mentioned above [41].

Despite having several potential advantages, GQI also has limitations. First of all, the measured SDF provided by GQI does not necessarily guarantee correct results unless the sampling scheme fulfills the balanced requirement. Second, the measured density function $\rho(\mathbf{r})$ in GQI is affected by T_1, T_2, and B1 inhomogeneity, resulting in errors between the measured density function and the actual one. However, there are possible ways to minimize these effects. The effect of T_1 can be minimized by choosing a longer TR, which is already used in diffusion MRI of the whole brain using current 2D EPI techniques. Eliminating the effect of T_2 is harder because in the pulsed-gradient spin-echo diffusion sequence, TE is approximately 100 ms for the current clinical scanners. A possible solution is to acquire an additional b0 image with a different TE. This additional b0 image can be used to estimate the effect of T_2 and to eliminate it. The effect of B1 inhomogeneity is noticeable on current 3T scanners, resulting in non-uniform excitation within an imaging slice. This effect could be mitigated by novel RF pulse designs which are under active development. Third, the measured SDF pattern is changed according to the sampling scheme used, as

noted in Figs. 2 and 3. This implies that the performance of GQI depends on the diffusion sampling scheme. Further study is required to develop an optimum sampling scheme within an acceptable scan time that offers the measured SDF closest to the actual SDF.

ACKNOWLEDGMENT

The authors would like to thank Dr. C.-P. Lin and Dr. K.-H. Cho for technical assistance in image acquisition at National Yang-Ming University.

REFERENCES

[1] M. Doran *et al.*, "Normal and abnormal white matter tracts shown by MR imaging using directional diffusion weighted sequences," *J. Comput. Assist. Tomogr.*, vol. 14, pp. 865–73, Nov.-Dec. 1990.

[2] M. E. Moseley *et al.*, "Early detection of regional cerebral ischemia in cats: Comparison of diffusion- and T2-weighted MRI and spectroscopy," *Magn. Reson. Med.*, vol. 14, pp. 330–46, May 1990.

[3] P. J. Basser, J. Mattiello, and D. LeBihan, "Estimation of the effective self-diffusion tensor from the NMR spin echo," *J. Magn. Reson. B*, vol. 103, pp. 247–54, Mar. 1994.

[4] P. J. Basser and C. Pierpaoli, "Microstructural and physiological features of tissues elucidated by quantitative-diffusion-tensor MRI," *J. Magn. Reson. B*, vol. 111, pp. 209–19, Jun. 1996.

[5] C. Pierpaoli, P. Jezzard, P. J. Basser, A. Barnett, and G. Di Chiro, "Diffusion tensor MR imaging of the human brain," *Radiology*, vol. 201, pp. 637–48, Dec. 1996.

[6] C. Pierpaoli and P. J. Basser, "Toward a quantitative assessment of diffusion anisotropy," *Magn. Reson. Med.*, vol. 36, pp. 893–906, Dec. 1996.

[7] M. R. Wiegell, H. B. Larsson, and V. J. Wedeen, "Fiber crossing in human brain depicted with diffusion tensor MR imaging," *Radiology*, vol. 217, pp. 897–903, Dec. 2000.

[8] A. L. Alexander, K. M. Hasan, M. Lazar, J. S. Tsuruda, and D. L. Parker, "Analysis of partial volume effects in diffusion-tensor MRI," *Magn. Reson. Med.*, vol. 45, pp. 770–80, May 2001.

[9] D. S. Tuch *et al.*, "High angular resolution diffusion imaging reveals intravoxel white matter fiber heterogeneity," *Magn. Reson. Med.*, vol. 48, pp. 577–82, Oct. 2002.

[10] T. Hosey, G. Williams, and R. Ansorge, "Inference of multiple fiber orientations in high angular resolution diffusion imaging," *Magn. Reson. Med.*, vol. 54, pp. 1480–9, Dec. 2005.

[11] S. Peled, O. Friman, F. Jolesz, and C. F. Westin, "Geometrically constrained two-tensor model for crossing tracts in DWI," *Magn. Reson. Imag.*, vol. 24, pp. 1263–70, Nov. 2006.

[12] E. Özarslan and T. H. Mareci, "Generalized diffusion tensor imaging and analytical relationships between diffusion tensor imaging and high angular resolution diffusion imaging," *Magn. Reson. Med.*, vol. 50, pp. 955–65, Nov. 2003.

[13] C. Liu, R. Bammer, B. Acar, and M. E. Moseley, "Characterizing non-Gaussian diffusion by using generalized diffusion tensors," *Magn. Reson. Med.*, vol. 51, pp. 924–37, May 2004.

[14] D. C. Alexander, G. J. Barker, and S. R. Arridge, "Detection and modeling of non-Gaussian apparent diffusion coefficient profiles in human brain data," *Magn. Reson. Med.*, vol. 48, pp. 331–40, Aug. 2002.

[15] A. W. Anderson, "Measurement of fiber orientation distributions using high angular resolution diffusion imaging," *Magn. Reson. Med.*, vol. 54, pp. 1194–206, Nov. 2005.

[16] Y. Assaf, R. Z. Freidlin, G. K. Rohde, and P. J. Basser, "New modeling and experimental framework to characterize hindered and restricted water diffusion in brain white matter," *Magn. Reson. Med.*, vol. 52, pp. 965–78, Nov. 2004.

[17] Y. Assaf and P. J. Basser, "Composite hindered and restricted model of diffusion (CHARMED) MR imaging of the human brain," *Neuroimage*, vol. 27, pp. 48–58, Aug. 2005.

[18] J. H. Jensen, J. A. Helpern, A. Ramani, H. Lu, and K. Kaczynski, "Diffusional kurtosis imaging: The quantification of non-gaussian water diffusion by means of magnetic resonance imaging," *Magn. Reson. Med.*, vol. 53, pp. 1432–40, Jun. 2005.

[19] H. Lu, J. H. Jensen, A. Ramani, and J. A. Helpern, "Three-dimensional characterization of non-gaussian water diffusion in humans using diffusion kurtosis imaging," *NMR Biomed.*, vol. 19, pp. 236–47, Apr. 2006.

[20] L. Minati *et al.*, "Biexponential and diffusional kurtosis imaging, and generalised diffusion-tensor imaging (GDTI) with rank-4 tensors: A study in a group of healthy subjects," *Magn. Reson. Materials Phys., Biol. Med.*, vol. 20, pp. 241–53, Dec. 2007.

[21] J. D. Tournier, F. Calamante, D. G. Gadian, and A. Connelly, "Direct estimation of the fiber orientation density function from diffusion-weighted MRI data using spherical deconvolution," *Neuroimage*, vol. 23, pp. 1176–85, Nov. 2004.

[22] E. Kaden, T. R. Knosche, and A. Anwander, "Parametric spherical deconvolution: Inferring anatomical connectivity using diffusion MR imaging," *Neuroimage*, vol. 37, pp. 474–88, Aug. 2007.

[23] J. D. Tournier, F. Calamante, and A. Connelly, "Robust determination of the fibre orientation distribution in diffusion MRI: Non-negativity constrained super-resolved spherical deconvolution," *Neuroimage*, vol. 35, pp. 1459–72, May 2007.

[24] E. Kaden, A. Anwander, and T. R. Knosche, "Variational inference of the fiber orientation density using diffusion MR imaging," *Neuroimage*, vol. 42, pp. 1366–80, Oct. 2008.

[25] S. Mori and P. C. van Zijl, "Fiber tracking: Principles and strategies – A technical review," *NMR Biomed.*, vol. 15, pp. 468–80, Nov.-Dec. 2002.

[26] P. T. Callaghan, *Principles of Nuclear Magnetic Resonance Microscopy*. Oxford, U.K.: Clarendon, 1993, pp. 438–441.

[27] D. S. Tuch, "Q-ball imaging," *Magn. Reson. Med.*, vol. 52, pp. 1358–72, Dec. 2004.

[28] D. S. Tuch, T. G. Reese, M. R. Wiegell, and V. J. Wedeen, "Diffusion MRI of complex neural architecture," *Neuron*, vol. 40, pp. 885–95, Dec. 2003.

[29] L. W. Kuo *et al.*, "Mossy fiber sprouting in pilocarpine-induced status epilepticus rat hippocampus: A correlative study of diffusion spectrum imaging and histology," *Neuroimage*, vol. 41, pp. 789–800, Jul. 2008.

[30] C. P. Hess, P. Mukherjee, E. T. Han, D. Xu, and D. B. Vigneron, "Q-ball reconstruction of multimodal fiber orientations using the spherical harmonic basis," *Magn. Reson. Med.*, vol. 56, pp. 104–17, Jul. 2006.

[31] M. Descoteaux, E. Angelino, S. Fitzgibbons, and R. Deriche, "Regularized, fast, and robust analytical Q-ball imaging," *Magn. Reson. Med.*, vol. 58, pp. 497–510, Sep. 2007.

[32] V. J. Wedeen, P. Hagmann, W. Y. Tseng, T. G. Reese, and R. M. Weisskoff, "Mapping complex tissue architecture with diffusion spectrum magnetic resonance imaging," *Magn. Reson. Med.*, vol. 54, pp. 1377–86, Dec. 2005.

[33] V. J. Wedeen *et al.*, "Diffusion spectrum magnetic resonance imaging (DSI) tractography of crossing fibers," *Neuroimage*, vol. 41, pp. 1267–77, Jul. 2008.

[34] A. Barnett, "Theory of Q-ball imaging redux: Implications for fiber tracking," *Magn. Reson. Med.*, vol. 62, pp. 910–23, Oct. 2009.

[35] P. Hagmann *et al.*, "Fibertract segmentation in position orientation space from high angular resolution diffusion MRI," *Neuroimage*, vol. 32, pp. 665–75, Aug. 2006.

[36] L. W. Kuo, J. H. Chen, V. J. Wedeen, and W. Y. Tseng, "Optimization of diffusion spectrum imaging and q-ball imaging on clinical MRI system," *Neuroimage*, vol. 41, pp. 7–18, May 2008.

[37] H. Gudbjartsson and S. Patz, "The Rician distribution of noisy MRI data," *Magn Reson Med.*, vol. 34, pp. 910–4, Dec. 1995.

[38] P. J. Basser, S. Pajevic, C. Pierpaoli, J. Duda, and A. Aldroubi, "In vivo fiber tractography using DT-MRI data," *Magn. Reson. Med.*, vol. 44, pp. 625–32, Oct. 2000.

[39] M. H. Khachaturian, J. J. Wisco, and D. S. Tuch, "Boosting the sampling efficiency of q-Ball imaging using multiple wavevector fusion," *Magn. Reson. Med.*, vol. 57, pp. 289–96, Feb. 2007.

[40] Y. C. Wu and A. L. Alexander, "Hybrid diffusion imaging," *Neuroimage*, vol. 36, pp. 617–29, Jul. 2007.

[41] F. C. Yeh, V. J. Wedeen, and W. Y. Tseng, "Practical crossing fiber imaging with combined DTI datasets and generalized reconstruction algorithm," presented at the Proc. 17th Meeting Int. Soc. Magn. Reson. Med. (ISMRM), Honolulu, HI, 2009.